On the detection of nanoparticle cloud migration by a resonant photonic surface signal towards sedimentation velocity measurements

L. Garnier, J. Gastebois, H. Lhermite, V. Vié, Arnaud Saint-Jalmes, H. Cormerais, E. Gaviot, Bruno Bêche

Results in Optics 12 (2023) 100430

Contents lists available at ScienceDirect

Results in Optics

journal homepage: www.sciencedirect.com/journal/results-in-optics

On the detection of nanoparticle cloud migration by a resonant photonic surface signal towards sedimentation velocity measurements

L. Garnier [a], J. Gastebois [a], H. Lhermite [a], V. Vié [b], A. Saint-Jalmes [b], H. Cormerais [a,c], E. Gaviot [d], B. Bêche [a,*]

[a] Univ Rennes, CNRS, IETR (Institut d'Electronique et de Technologies numéRiques) – UMR 6164, F-35000 Rennes, France
[b] Univ Rennes, CNRS, IPR (Institut de Physique de Rennes) – UMR 6251, F-35000 Rennes, France
[c] Centrale/Supelec, Campus de Rennes, F-35510 Cesson-Sévigné, France
[d] Le Mans Université, CNRS, LAUM (Laboratoire d'Acoustique) – UMR 6613, F-72000, France

ARTICLE INFO

Keywords:
Nanoparticle migration
Fragmented material
Sedimentation rate
Integrated photonic devices
Surface resonant signal
Real time signal processing
Optoelectronic detection

ABSTRACT

Migration and sedimentation of solid particles in a liquid are physical phenomena involving accumulation of soft matter or decantation of fragmented matter. A thorough understanding together with relevant measurements are prerequisites regarding many fields, including medicine, galenic pharmacology, food processing, and the cosmetics industry. In this paper, we investigate the feasibility of monitoring and detecting the migration of a nanoparticle cloud with a resonant light probe. For this purpose, hybrid silicon/silica/UV210 organic integrated photonic racetrack resonators were patterned by thin film processes to be used as sensors measuring the outcome of the impact of a cloud of nanoparticles, the dynamic migration plus sedimentation phenomenon of the nanoparticle cloud in water. A broadband superluminescent diode has been used for the excitation. Then, the spectral characteristics of the resonant guided modes have been analyzed, considering the observed changes while tracking the free spectral range of the transduced comb spectra as a function of time. The way to operate can be summarized as follows: Solutions based on spherical silica nanoparticles of fixed size are prepared and subjected to rheological measurements to obtain their respective viscosities. Next, a millimeter tank filled with water is conveniently placed on the active surface of the sensing chip, prior to the addition of one of the previously mentioned solutions. The series of spectra are acquired during the whole migration sequence and the transduced optical signal is then directly processed and treated by a specific code operated in real time by way of Lagrange interpolation polynomials. Collected data are then compared to a simple theoretical model describing the sedimentation of a spherical particle in water (Stokes' law). Eventually, the implementation of the device in a characterization platform and the development of a specific protocol allows a global treatment, whose description is followed by discussions on measurements and data. Consequently, after the impact of the drop containing the nanoparticles, the monitoring of a first phase regarding their fast cloud migration into the global study volume (with flow of matter plus vortex) eventually followed by their slow sedimentation, can be detected using such a resonant light probe. The overall duration of the first phase associated with sedimentation velocities is in the order of a few tens of μm/min for particles with submicron diameters (several hundreds of nanometers); a first attempt of comparison of this first phase with the results of the classic Stokes model would give a convergence of the values reaching between 9 and 19% for the sedimentation rates.

1. Introduction

Many universal processes of migration, sedimentation and decantation of suspensions are widely observed in the fields of physical, chemical sciences and engineering (Blazy et al., 1999; Blazy and Jousset, 2011; Tee et al., 2002). Considering suspensions and fragmented matter, the settling of particles in various liquids involves physical mechanisms due to the properties of the liquid needing to be understood and measured in many cases. Relevant measurements are critical prerequisites in many fields including medicine, galenic pharmacology (drugs with active substances suspended in colloids), food processing, cosmetics industry, energy industry, sludge treatment industry and so

* Corresponding author.
E-mail address: bruno.beche@univ-rennes.fr (B. Bêche).

https://doi.org/10.1016/j.rio.2023.100430
Received 5 November 2022; Received in revised form 13 March 2023; Accepted 4 April 2023
Available online 7 April 2023

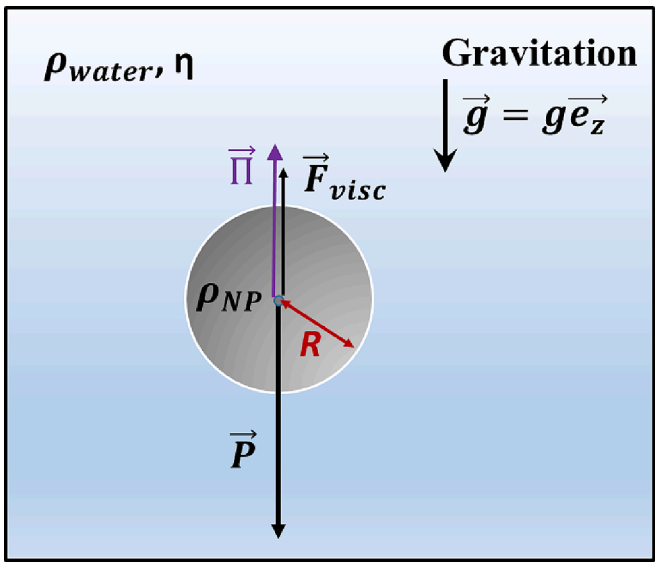

Fig. 1. Schematic representation of a spherical particle during sedimentation. The nano-particle (NP) of volumic mass ρ_{NP} and radius R immersed in a fluid of volumic mass ρ_{water} and dynamic viscosity η in a gravitational field $\vec{g}$, is subject to: its weight, the Archimede's force $\vec{\Pi}$, and the viscous friction force $\vec{F}_{visc}$. In the special case of spherical geometry of the particle, such a drag force is called the Stokes force.

on. For instance, with medical diagnosis, the accurate knowledge of the sedimentation speed of red blood cells allows an early diagnosis for various inflammations; indeed, in such cases, the presence of specific proteins causes red blood cells to aggregate, increasing so their sedimentation speed. Sedimentation rate measurements are also of great importance in the oil industry. Petroleum products contain impurities that, if present in the final product, can cause serious damage. For example, solid sediments or mineral ashes can clog filters, wear out mechanical parts of combustion chambers and trigger bacteriological problems. The turbidity of a suspension is also strongly correlated to sedimentation processes and linked in many applications to the validity and quality of a product (Pelletier, 2009).

Historically, numerous methods and principles based on wave/matter interactions have been developed to probe sedimentation and deposition processes. Many of these techniques are associated with volume measurements and rely on the use of different wavelengths with: X-rays (Aidi et al., 1989), acoustics, ultrasound (Razavian et al., 1997; Nam et al., 2012) and optics (Midelet et al., 2017). While investigating such dynamic changes within the substance and its suspension, the principles of detection may involve different attributes of the wave (Cipelletti and Ramos, 2002; Bissig et al., 2003): namely, its amplitude (intensity and absorption) and its ability to interfere (coherence) by way of interferometric methods (Razavian et al., 1997), specific modulation

Table 1
Plasma and photolithography procedure and thin layer processes for the fabrication of the global photonic circuit.

Steps		Parameters
Pre-exposure	Thermal oxidation	4 h min at 1175 °C, successively
	Humid pyrolitic	O_2 (2 l/min) + N_2 (2 l/min) 5 min
	oxidation	O_2 (2 l/min) 10 min
	(SiO_2, AET Technologies)	H_2 (1.8 l/min) + O_2 (1 l/min) 4 h
		N_2 (2 l/min) 20 min
	Spin-coating, UV210	V = 900 rpm, a = 5000 rpm/s, t = 30 s
	Thickness, roughness	850–900 nm, < 2 nm
	Softbake	3 min at 140 °C
Exposure	Deep UV	E = 20 mJ/cm^2, t = 27 s
	Soft-bake	1 min at 120 °C
Post-exposure	Development	30 s, with Microposit MF CD-26
	Softbake	24 h at 120 °C

principles, spectroscopy analyses and resonance phenomena (Hallil et al., 2021); in such cases the wave brings out information considering measurements based on its specific nature. This study aims to develop and take advantage of a quasi-surface measurement technique that relies on the quantized characteristic of a resonant optical light wave to probe a given sedimentation process above its location. In this context, the guided light stems from resonators acting as a carpet of localized light with a view to probing the upper volume of suspension subjected to sedimentation dynamics. Thus, the quantified signal and its spectral variation during sedimentation provide information about these dynamics. Micro-resonators (MRs) have been widely studied over the past few decades, both in telecommunications (Rabus, 2007; Rabiei et al., 2002), micro-lasers pedestals (Reynoso-De La Cruz et al., 2021) and sensors applications (Vollmer and Arnold, 2008; Su, 2015; Xu et al., 2010).

Most of the sensors applications concerning these devices focus on the detection of biochemical species and the measurement of their concentration (Chao et al., 2006; Delezoide et al., 2012; Schweinsberg et al., 2006) for environmental applications (Schweinsberg et al., 2006). Such measurements address the detection of glucose (Castro-Beltrán et al., 2015) or heavy metal pollutants (Meziane et al., 2015) in a medical and biological context (Qavi and Bailey, 2010; Qavi et al., 2011). In addition to detections and concentration measurements, MRs have also been used to determine the phase transition temperature with specific biological compounds (Li et al., 2017; Castro-Beltrán et al., 2020). However, only a few studies have been performed to follow a dynamic process occurring in the immediate vicinity of the resonator over time. Many mechanisms concerning soft matter (sedimentation, flocculation, drying, and other effects) are also slow enough to be controlled in the food cosmetics fields, considering suspensions, colloids and gels (Manley et al., 2005; Le Floch-Fouéré et al., 2019; Lanotte et al., 2018; Yu et al., 2021). At a given wavelength, a micro-resonator (MR) is characterized by its eigenvalue, namely the effective index n_{eff}^{phase} of an optical mode propagating inside and belonging to the cone of light defined by the wave vector relation of the waveguide $k_0.n_{cladding} \leq k_0.n_{eff}^{phase} \leq k_0.n_{core}$. According to the eigenvalues equation derived from the solution of Maxwell's equations, the effective index n_{eff}^{phase} depends on the opto-geometric characteristics of the resonator, as well as its close environment (Delezoide, 2012). Thus, as far as resonance is concerned, a progressive change in this environment entails a temporal variation of the effective index.

In this study, we use specific organic MRs (Rohm and Haas Electronic Materials, 2005; Duval et al., 2010), featuring prominent probing vanishing tail characteristics due to the low value of the organic index material: then we can follow the dynamic phenomenon of migration and sedimentation of a nanoparticle cloud in water after the impact against this optically resonant surface: the consequences on the spectral characteristics of the guided mode located onto the surface are thus analyzed. To this end, racetrack-shaped MRs are integrated on a chip by means of photolithography before being stimulated by a broadband laser or superluminescent diode. The transduced optical signal is then directed to an Optical Spectrum Analyzer (OSA) or simple spectrometer where the spectral information is acquired as a function of time, the signal being processed in real time. To this end, a millimeter tank filled with water is appropriately deposited on the surface of the chip, before adding the nanoparticle solution under test. Then, during the whole sedimentation process spectra are acquired, and collected data are compared to a simple theoretical model describing the sedimentation of a spherical particle in water.

The second part of the article presents respectively the basic fluid theory and how to obtain the sedimentation rate of a spherical particle plus the optical resonance aspect. Then, section three is devoted to the presentation of the materials and the thin layer processes together with the procedure yielding the overall experimental setup; this, from the fabrication of the photonic structure by photolithography to the

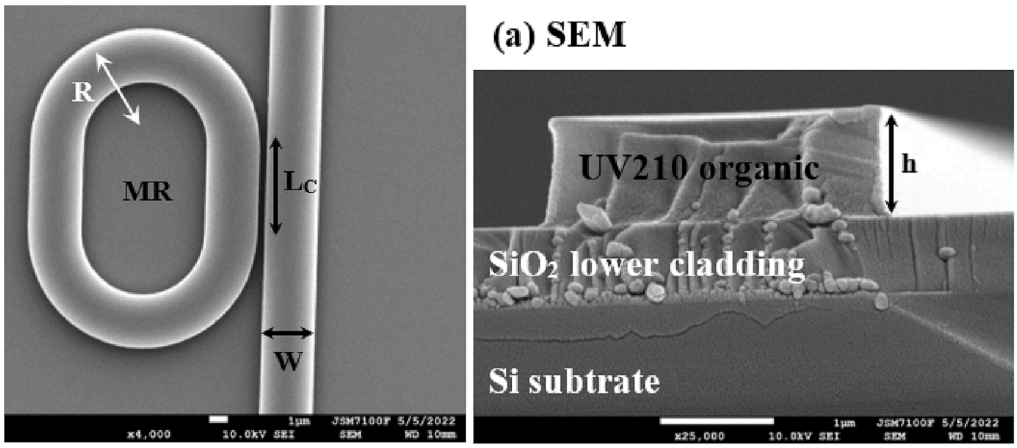

Fig. 2. (a) Scanning electron microscopy (SEM) imaging of the top view of a resonator element plus the cross-sectional view of the waveguide structure (Si/SiO_2/UV210). R = 5 μm is the radius of curvature of the curved part of the micro-resonator, L_c = 5 μm the coupling length between the resonator and the access waveguide, and w = 3 μm is the waveguide width. It should be noted that the height h of the guide obtained by the fabrication described in Table 1 is 0.9 μm. (b) Characterization platform sketch. The photonic circuit is excited by means of a broadband laser diode (SUPERLUM SLD-331) of central wavelength λ_0 = 795 nm and full width at half maximum FWHM = 40 nm. The mode is then polarized and isolated in order to avoid any back reflection. Two microscope objectives are then positioned to inject the light in the photonic structures in one hand, and to defocalize it in the other hand. After defocalization, the light is directed to a beam-splitter to be redirected to a CCD camera (PulNix) so as to monitor the injection, and to an Optical Spectrum Analyzer (OSA, ANDO AQ-6315E) or spectrometer (Ocean Optics HR4000) driven by an own Matlab computer program for the acquisition of the transduced spectra, FFT calculation plus Lagrange's polynomial simulation onto the peak to obtain FSR. The photonic chip, and both microscope objectives are placed on piezoelectric nano-positioners in order to maximize the precision of the injection. Below, an optical microscopy imaging (obj. ×20) of the four resonators used as the sensing area. The four racetrack-shaped micro-resonators are coupled to an access waveguide and a taper structure is arranged at the input of the latter so as to facilitate the injection by spatially compressing the guided mode. The resonant elements extend over a typical distance of 150 μm.

inclusion of the device in an optical characterization platform. Data acquisition, signal processing and specific treatments are also described. Experimental results regarding the first set of measurements, performed according to the outlined resonant principles, are analyzed and discussed, before being corroborated by a volume optical imaging in the fourth section. The fifth section concludes such study.

2. Elementary aspects in fluid and optics for the experiment

2.1. Fluid aspect, migration of fragmented matter, sedimentation

Sedimentation phenomena can be considered as part of a field concerning the dynamics of soft matter (De Gennes et al., 2005; Cabane and

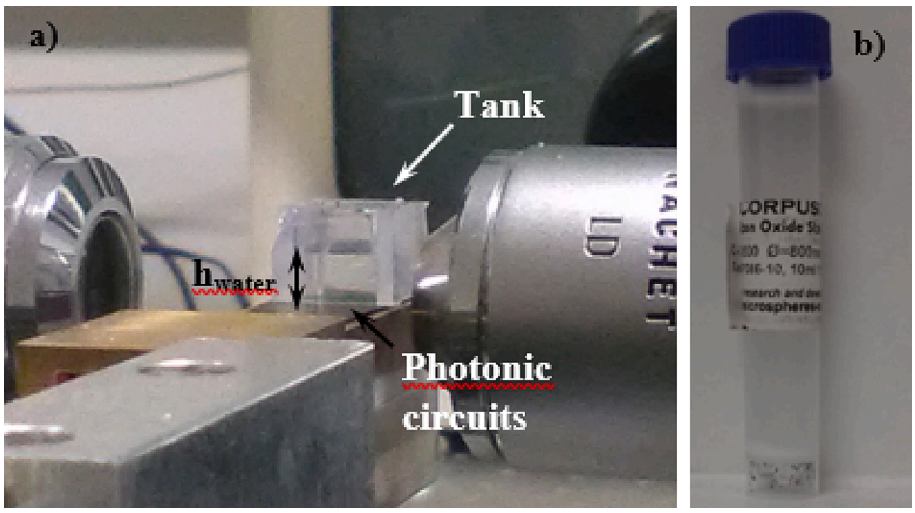

Fig. 3. (a) Photographs of the two microscope objectives used for the injection and of the photonic chip. A millimeter tank is stuck on the top of the chip and filled with water to perform the sedimentation measurements; h_{water} represents the height of the volume water; experimentally this value was taken to 2, 3 and 4 mm for various successive measurements. (b) Photograph of the aqueous suspension of silica nano-particles.

Hénon, 2007). As mentioned earlier, these phenomena are present at different scales, both geological and planetary as well as microscopic, for a wide range of applications (Blazy et al., 1999; Blazy and Jousset, 2011). Sedimentation is a phenomenon describing the fall of a mass of matter in a fluid medium. The sedimentation of a spherical nano-particle (NP) in liquid water is depicted in Fig. 1 according to a classical scheme. The sedimentation rate (settling velocity) of a given particle is obtained by applying Newton's second law on the particle considering its weight, Archimedes' principle and the viscous friction force. This procedure leads to a well-known analytical expression of the sedimentation velocity called Stokes velocity. Thus, considering a spherical ball into pure water, $v_{Stokes} = \frac{2}{9}\frac{gR^2(\rho_{NP}-\rho_{water})}{\eta_{water}}$. For our experimental conditions, the two parameters $\rho_{NP} = 2650\ kg/m^3$ and $\rho_{water} = 1000\ kg/m^3$ represent the volumetric mass (density) of the silica nanoparticle and water fluid, respectively: R is the radius of the spherical particles, $g = 9.81\ m/s^2$ the gravitational acceleration and η_{water} the dynamic viscosity of the water fluid. This theoretical expression may be applied for silica nano-particles (NPs) of different sizes (radius $R = R_{particles} = 250$, 300 and 400 nm) during their sedimentation in water for the considered measurements. The experiments presented below were performed with solutions containing a large amount of nano-particles (Corpuscular Inc., NPs with a concentration 10 mg/mL), subsequently forming a cloud of fragmented material under sedimentation. The previous model based on Newton's second law is only relevant for a single particle because it does not take into account collective effects, such as the change in effective Einstein viscosity caused by the presence of many nano-particles. However, at a first order we can use it for simplicity and homage to G.G. Stokes (Stokes, 1851). As a simple theory, it allows us in all cases to validate our experimental measurements involving resonant light probes, which is the goal of any relevant experimental study in applied physics. However, it should be noted that other models exist modifying this first approach: such models (applied by A. Einstein) can take into account an apparent (or effective) viscosity $\eta_{eff} = \eta_{water}(1 + 2.5\ \Phi)$, greater than that of the liquid water η_{water} when the fraction volume Φ of NPs is increased. This naturally leads to possible corrections on the migration processes, sedimentation being able to result in the modified average velocities expressed as $< v > = v_{Stokes}.f(\Phi)$, with a specific function $f(\Phi)=(1- \Phi)^n$ and n a numerical experimental factor (Richardson and Zaki, 1954). Considering this first study of possible detection of the impact of a drop containing nanoparticles (NPs) against a resonant optical surface (for detecting their migrations and sedimentations), we have chosen to start from the first and basic law of Sir Stokes by simplicity for a preliminary approach for the phenomenon. In addition, we corroborate the result with an optical volume image of the complete process showing the bursting of the drop filled with NPs before the NPs distribution in real time.

2.2. Optical resonance aspect

Surface resonant light probes consist of photonic micro-resonators (MRs) arranged under the dynamic process of nanoparticle (NP) migration and sedimentation. The surface resonant elements can thus create the localized resonant light or probe. Inside a resonator, only waves called whispering gallery modes, that present phase accordance after one round, can circulate. Applying the resonance condition to two consecutive values of relevant resonant wavelengths, the spectral separation $\Delta\lambda$ between two wavelengths is called Free Spectral Range (FSR). In our case, the experiments are conducted with a broad-spectrum source: then such a light is assigned with the effective group index n_{eff}^{group} of the whole structure taking into account the whole dispersion aspect. This effective index accounts for the group velocity of the light wave package, which is more relevant for broadband sources. A first order expansion of Taylor-Lagrange is adequate to properly describe the overall modal dispersion (Delezoide, 2012) that can be written $n_{eff}^{group}(\lambda) = n_{eff}^{phase}(\lambda_0) - \lambda.\frac{dn_{eff}^{phase}}{d\lambda}$. With the above considerations and the use of a broadband source to probe the resonators, two dispersive contributions are simultaneously added: at first, the physical dispersion of the materials (including the one of the UV210 organic that is particularly pronounced in the intense red radiation), then the modal dispersion contribution which is specific to the mathematical non-linearities of the dispersion curves with such guiding resonant structures. It is therefore this overall effective group index that must be taken into account in the resonance parameters of the structures (Free Spectral Range FSR). Then, the variation detected over the resonators can be evaluated by tracking the pseudo-period (or Free Spectral Range, FSR) of the transduced spectra against time that verifies: $FSR = \Delta\lambda = \frac{\lambda_0^2}{P.n_{eff}^{group}}$: here, λ_0 is the excitation wavelength, P the geometrical perimeter of the resonator, and n_{eff}^{group} represents the previously mentioned whole effective group index, which should not be confused with the group index of the material.

3. Materials and thin layer processes, experimental set up and relevant procedure

3.1. Materials, chemical aspect and resin, thin layer processes

Before experiments, such micro-structures have been designed with Cadence Virtuoso software, the fabrication involving then quartz/

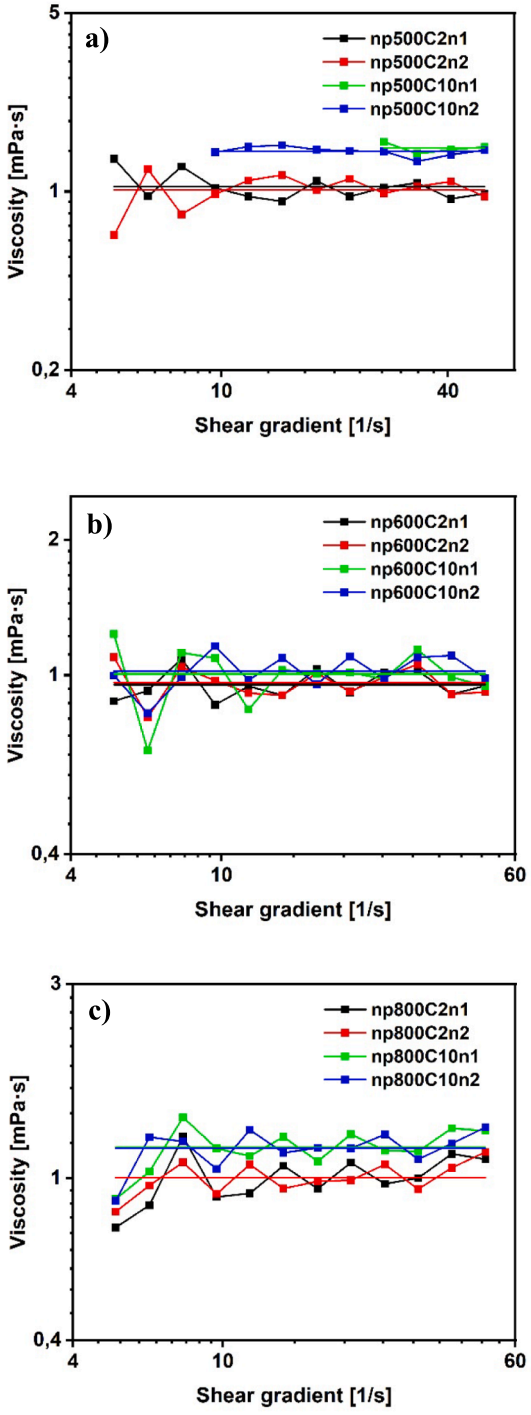

Fig. 4. Rheology aspect: measurements of the viscosities of 'water + nanoparticle (NP) 'mixtures, for two concentrations [C] = 2 and 10 mg/ml and three sizes of NP, by the rheometer (Anton Paar MCR 301): (a) diameter $D = 2R_{part}$ = 500 nm, (b) 600 nm and (c) 800 nm. Statistics and dispersion over two successive tests. Tests and corresponding colored measurement curves are noted "np Dvalue Cvalue numtest". For this type of 'mechanical' rheology measurements typically 1 ml of such mixture of 'water + NP' are required.

chromium masks (TOPPAN PHOTOMASK Inc.). This highlights the microtechnological aspects of this study that allowed the realization of this specific sensor as a chip whose parts are produced by thin film deposits and photolithography processes. Thus, the circuits are fabricated in UV210, a polymer with an absorption band at 248 nm in the deep-UV range which allows us to perform deep-UV photolithography. Such a process operating at 248 nm enables the design of more precise and smaller structures than the traditional 'i-line' photolithography performed at 365 nm. First a thermal silica layer is formed on a silicon substrate by wet oxidation method. Before, the wafer needs to be cleaned with the RCA method (developed by 'Radio Company of America'), to avoid all kinds of impurities. Then the plate is put in a quartz furnace with torch, the gas H_2 and oxidation gas O_2 being located in the flame to ensure combustion. A step lasting typically 4 h in an oven at 1175 °C can form a typically 1 μm layer of silica on the wafer surface, creating then the silica lower cladding. After oxidation, a mandatory annealing at 700 °C-800 °C strengthens the single crystal structure. Such a thickness value secures a highly stable and homogeneous refractive index regarding the organic waveguides and MRs, so as to reduce any loss of optical radiation from the propagation modes. Then the UV210 resin is spread on the surface of a thermally oxidized Si wafer using the spin-coating technique. Indeed, once the substrate/cladding is achieved, the organic patterns are grown and shaped by way of specific processes involving deep UV lithography tailored to the DUV210 polymer which is an amplified chemical resist material. The photolithography process is performed using a mask aligner (MJB4 Mask Aligner Suss MicroTec), along with a mercury lamp (HBO 1000 W/D, OSRAM) fitted with the appropriate filter to select the $\lambda = 248$ nm wavelength. Once the illumination is completed, the set of circuits can be developed with tetramethyl ammonium hydroxide (Microposit MF CD-26). It may be noted that the DUV210 polymer consists of poly p-hydroxystyrene (PHS) and poly t-butyl acrylate (PBA): it is called an amplified chemical photoresist because it includes a specific photo acid generator (PAG) to increase the sensitivity to UV energy exposure considering the involved specific photolithography mechanisms. In fact, with the PAG the DUV exposure induces the production of a small amount of acid acting as a catalyst during the exposure. Then, thermal activation of this acid with post exposure baking causes the proton H^+ to act as a catalyst and unlock the group from the PHS. Then, the cascade of chemical modifications activated by the acid triggers a change of polarity of the polymer from a lipophilic to a hydrophilic state. This makes the PHS soluble in the exposed areas. Thus, DUV exposed areas become soluble in a basic developer such as the Microposit MF CD-26. Relevant integrated UV210 MRs photonic structures have been fabricated according to such appropriate procedures. The set of suitable and optimized processes, as well as the complete photolithography procedure (plus the UV210 material aspects also described on the website (Yu et al., 2021), are summarized in Table 1. Are respectively depicted in Fig. 2 (a), the scanning electron microscopy (SEM) imaging of the top view of a resonator element plus the cross-sectional view of the waveguide structure (Si/SiO_2/organic UV210). At the specific coupling area, waveguides (access plus MR) present a width $w = 3$ μm; the others dimensions of the MR are respectively the radius of curvature and the coupling length, $R_{res} = L_c = 5$ μm and the gap $g = 0.4$ μm; the perimeter of the MR may be written $P = 2.(\pi R_{res} + L_c)$. Moreover, the guide height obtained by the fabrication described in Table 1 is 0.9 μm. The four resonators are laterally coupled to an access waveguide featuring a tapered structure that spatially compresses the optical mode before being coupled to the resonators, as described in Fig. 2. In addition, an optical microscopy imaging (obj. ×20) of the four resonators used as sensing area is shown in Fig. 2 (b). The four racetrack-shaped micro-resonators are coupled to an access waveguide and a taper structure is arranged at the input of the latter so as to facilitate the injection by spatially compressing the guided mode. These resonant elements extend over a typical distance of 150 μm. Thus, on a surface of approximately (30 × 150) = 4500 μm^2, the impacts, migrations then NPs cloud compression and sedimentation can be averaged and detected on the acting surface.

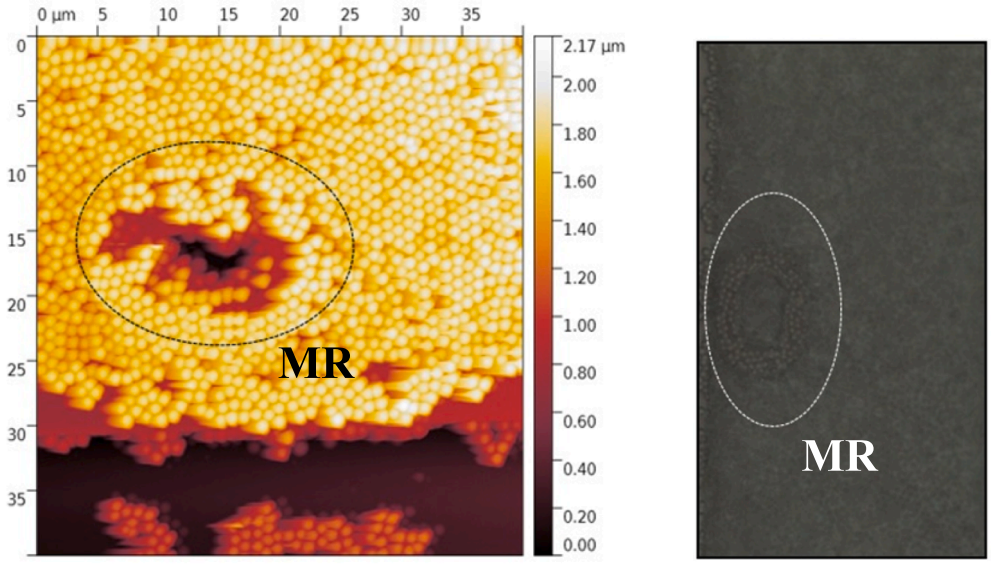

Fig. 5. (a) Atomic force microscopy and (b) optical microscopy imaging of the surface of the chip after sedimentation and total evaporation of the water contained in the tank. On both, one can distinguish the shape of the micro-resonator (MR) under the layers of nano-particles after complete drying.

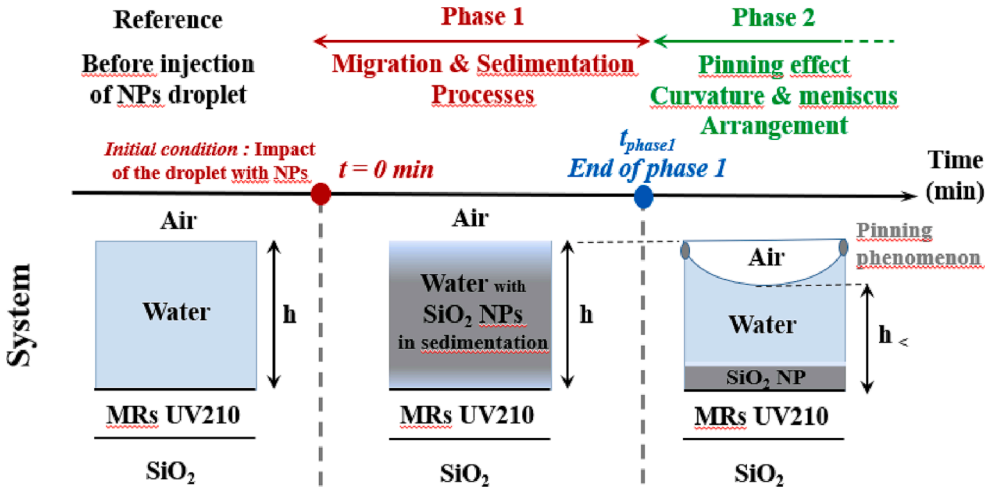

Fig. 6. Schematic representation of the global dynamic series of processes after the impact of the droplet with NPs into the tank: Phase 1, t = 0 min, migration and sedimentation of a cloud of nano-particles (NPs) in water down to the bottom. It forms a kind of cloud with a composite medium (mixture of NPs and water with vortex and gradients, Marangoni effect) regarding the surface resonant optical mode. The cloud of NPs concentrates on the background and the density of NPs increases; the thickness of the NPs layer shrinks until time t_{phase1} that represents the end of this first phase impact of the droplet/migration and sedimentation. Then a second phase begins with a specific increase in the curvature of the air/water interface with a pinning effect (NPs present at the triple points and edges of the tank on the surface). Due to such an effect, the nano-particles then organize, stabilize and stack, as one can see on Fig. 5 (a) and (b) after a long time, with sedimentation process and drying.

3.2. Experimental set up, optical/fluidic/nanoparticles (NPs), procedure and measurements

Once the set of available circuits is integrated on the wafer, the latter is cleaved with a diamond tip to be incorporated into a dedicated test platform to assess the free spectral range (FSR) values (Fig. 2 (b)). The resonator is excited by a broadband laser diode with a center wavelength λ_0 = 795 nm and a Gaussian spectrum 40-nm in width. To this end, microscope objectives are used to inject the light in the photonic circuit *via* the tapers and to defocus the output signal. The transduced signal is directed to an optical spectrum analyzer (OSA, Ando AQ-6315E) or a spectrometer (Ocean Optics HR4000) directly linked to a data acquisition system: then, a processing program developed in Matlab code with control of spectrometer and an interface human/machine is implemented. The broadband laser enables to visualize several resonances at the same time, in order to extract the Free Spectral Range (FSR), *i.e* the pseudo-period of the transduced spectrum.

A millimeter tank is positioned on the surface of the chip and filled with water (with fixed heights of 2 and 3 mm, according to the different statistic measurements), in order to perform the sedimentation experiments (Fig. 3 (a)). Once the tank is placed on the chip, the tested nanoparticles (NPs) suspension is added inside the tank by means of a microlitter pipette (Sartorius Proline Plus pipette, volume 5 µL consisting of NP silica mixture solution with a 10 mg/mL concentration).

Throughout each experiment the series of transduced spectra are acquired continuously with a Matlab data acquisition program implemented with the Optical Spectral Analyzer (OSA) or spectrometer (Ocean Optics HR 4000). A Fast Fourier Transform (FFT) calculation is performed from the recorded spectra to extract the FSR values by a Lagrange's interpolation around the peak of the FFT curve. Thus, when the FFT curve (its top) is digitized while involving three specific parameters α,β and γ (parabolic approximation), the classical Lagrange's interpolation allows to obtain the abscissa of the only one maximum value of the digitized FFT-peak, namely the FSR or period of the spectra.

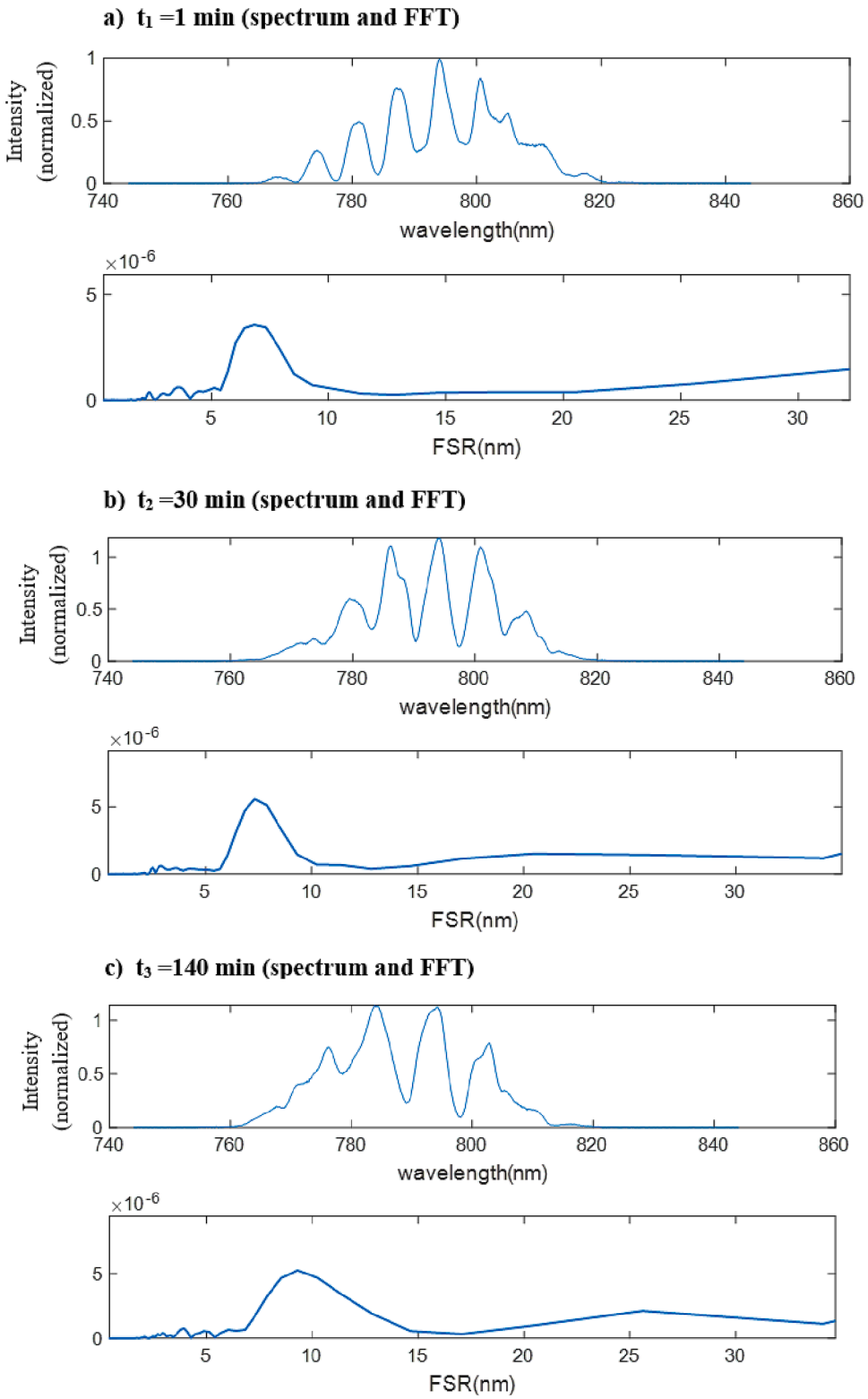

Fig. 7. Example of three spectra during the sedimentation process for nanoparticles with a radius R of 300 nm respectively at times *a)* $t_1 = 1$ min, *b)* $t_2 = 30$ min and *c)* $t_3 = 140$ min then their associated FFT curves. *d)* Diagram of the principle of calculating the FSR from an FFT curve: The FSR represents the pseudo-periods of the quantization which are directly calculated in real time by a 'Fast Fourier Transform' (FFT) type code with then the interpolations of the peaks of the FFT by a parabola or Lagrange's polynomial $\alpha\,(x_{FSR})^2 + \beta x_{FSR} + \gamma$. and determination of the coordinates of the peak of an FFT and therefore of its $x_{FSR\text{-}FFTpeak}$ abscissa called FSR. Typically, the relative variation of the FSR varies from factor 1 to 1.4 during the process. Proceeding in the same way for each time t_i during the sedimentation process *e)* Diagram of the evolution of FSR(t) over time *t* obtained for all the sedimentation experiments: a first phase of migration with vortex plus approaching the cloud of nanoparticles or sedimentation, then a second phase of arrangement associated with a form of statistical compression/densification of silica area to then stabilize. Note during phase 2 the increase in the curvature of the air/water interface with a pinning phenomenon at the triple points and edges of the tank.

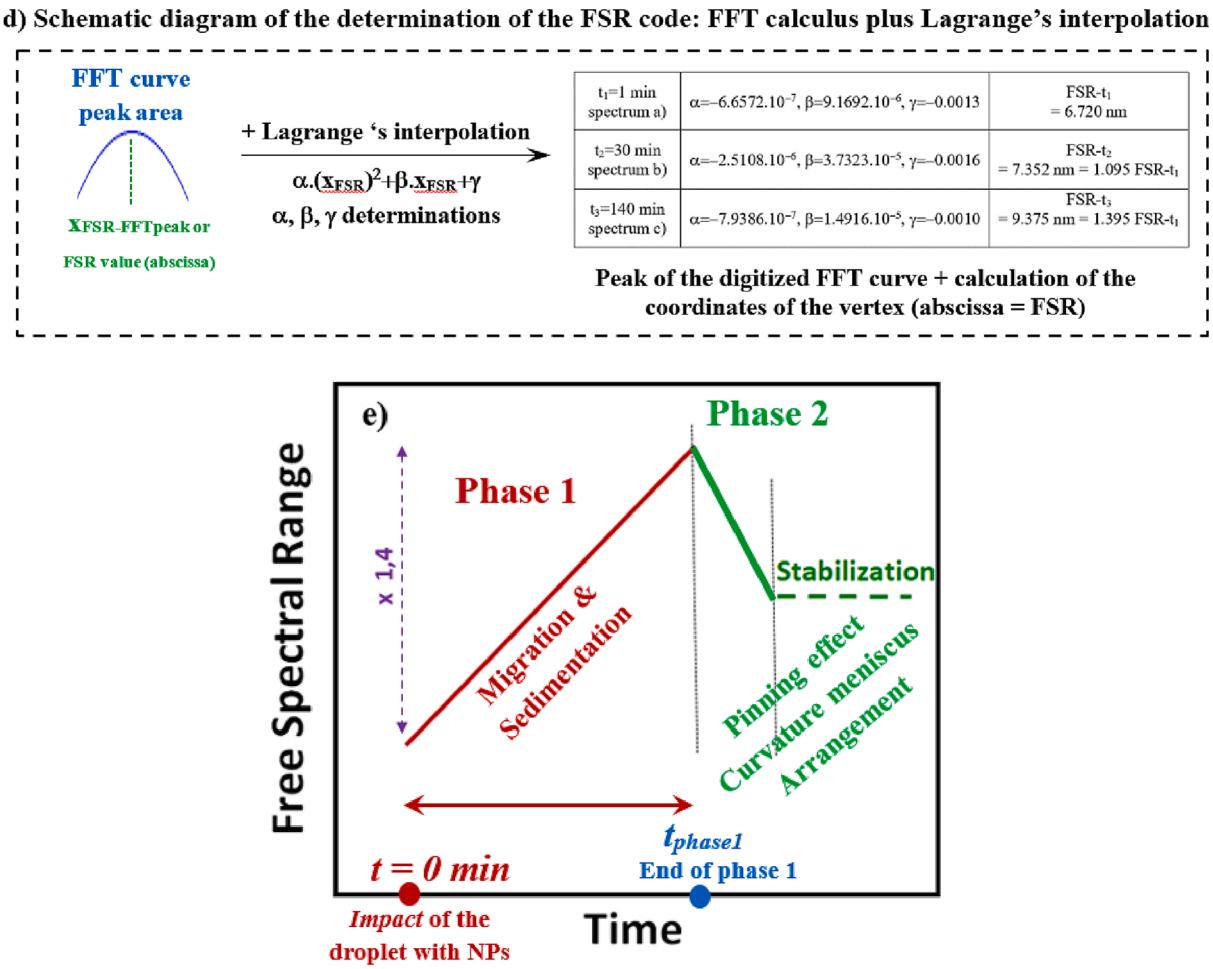

Fig. 7. (*continued*).

All of these steps are automated and work in parallel and in real time so as to get directly the FSR(t) curves while monitoring the whole process of the migrating and sedimenting NPs cloud. The FSR change associated with the resonant mode during respectively the impact, the migration into all the volume plus the sedimentation processes of silica nanoparticles (NPs) conducted above the photonic circuit will be test considering three particle sizes [R = 250 nm, 300 nm and 400 nm (Corpuscular Inc., NPs with a concentration of 10 mg/mL)]. Fig. 3 represents a photograph of both microscope objectives (used for the injection) together with the photonic chip. A millimeter tank is stuck on the top of the chip and filled with water to perform the sedimentation measurements: h_{water} represents the height of the water; experimentally this value was increased to 2, 3 and 4 mm for relevant successive measurements.

4. Experimental results, discussions and interpretations

4.1. Experimental results, viscosity and resonant optical measurements

Considering Stokes' law, the above-mentioned parameters (sedimentation rate, nanoparticles (NPs) radius R, viscosity) are closely related to each other. With a view to investigating a relevant operating mode to assess a given sedimentation rate linked to the resonant signal (considering the dynamic FSR(t): pseudo-period measurement of the spectrum), we must decorrelate specific parameters by measuring them independently with classical methods.

In this way we can first measure the viscosity of the water plus NPs mixture (Corpuscular Inc. silica NPs with respective concentrations of 10 mg/mL and 2 mg/mL obtained by dilution). Viscosity measurements by conventional mechanical or rheological methods are usually performed with a mixture of 1 or 2 ml of water + silica NPs, spread under a specifically shaped part rotating at a slowly increasing speed. Due to the advantageous configuration of the so-called "cone-plane" geometry of the Anton Paar MCR 301 rheometer (equipped with its rotating part) (GmbH, 2022), the observed thickness has its maximum value (0.9 mm) with a maximum radius at 2.5 cm of the rotating part. With a fixed rotation speed (rpm) of the rotating part, the "cone-plane" geometry has the most valuable following convenience. The shear rate (speed/thickness, *i.e.* s^{-1} in unit) remains uniform over the entire spread "water + NPs" sample mixture: indeed, as the radius of the rotating part increases, the speed of rotation also rises, but if the thickness also grows, then the shear rate remains constant over the entire puddle of spread mixture. Considering the shear rate values studied, the rotation of the part is almost imperceptible at the beginning and can reach 1 rpm at the end, which is very slow. Fig. 4 displays the measured viscosity values for different shear rates (the latter being expressed in s^{-1} and defined as the ratio of the plate displacement velocity divided by the fluid thickness). Are considered two concentrations [C] = 2 and 10 mg /mL and three NPs sizes (Anton Paar MCR 301): (a) diameter D = 2R = 500 nm, (b) 600 nm and (c) 800 nm. Statistically, two measurements were performed on each sample. The tests and corresponding colored curves are noted as "np Dvalue Cvalue numtest" in Fig. 4. For this kind of mechanical rheology measurements, typically a few ml of "water + NP" mixture is required. It is clear that the overall viscosity of these mixtures and particle concentrations tends towards the viscosity of water, *i.e.* 1 mPa.s. In addition, it appears that the viscosity of said mixtures appears

to increase very slightly as concentration is increased from 2 to 10 mg/mL.

Finally, while monitoring the sedimentation dynamics of NPs by electromagnetic signal of resonant light, the viscosity of the liquid medium (Fig. 1) may be considered as identical to that of water, i.e. 1 mPa.s (Fig. 4). Such photonic measurements were also performed in a tank (Fig. 3 (a)) containing 168 µL of pure water (corresponding to h = 3 mm), with the addition of only 5 µL of a 'water + NP' mixture at a concentration of 10 mg/mL at the beginning of the experiment. MRs displaying their surface resonant signal are placed underneath the tank where the sedimentation process takes place. Thus, in addition to the rheological measurements of the sedimentation phase (Fig. 4) and especially in view of the proportions during experiments and measurements with the resonant surface probes, it seems natural to fix the viscosity to that of water. Resonant photonic measurements of the NPs sedimentation process in water (solvent) were performed over typical times of 200 to 250 min, considering the signal processing described by the previous protocol. Fig. 5 (a) and (b) represent atomic force microscopy (AFM) and then optical microscopy imaging of the deposited NPs at the end of the sedimentation and drying process above the microresonators, respectively.

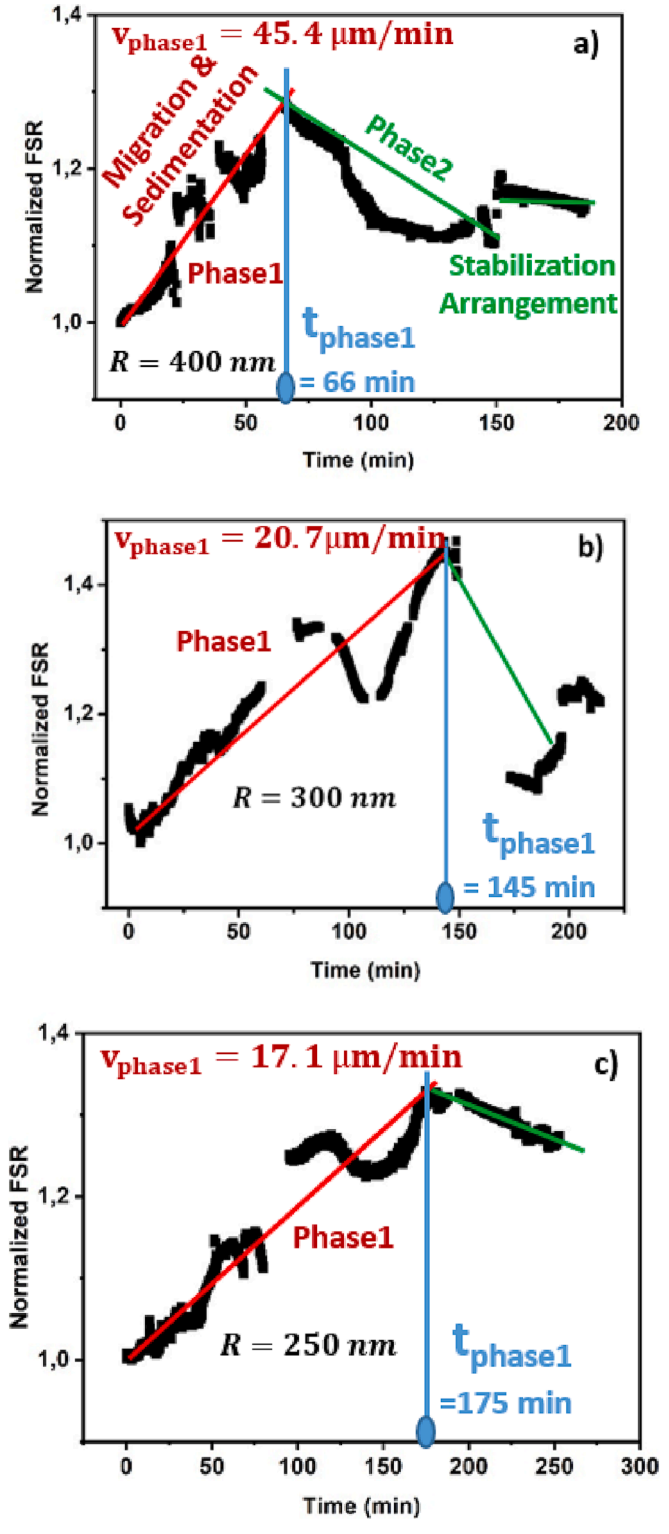

(caption on next column)

Fig. 8. Temporal evolution of the normalized FSR during the global impact, migration plus sedimentation process for spherical silica nanoparticles (NPs) of radius (a) R = 400 nm and h_{water} = 3 mm, (b) R = 300 nm and h_{water} = 3 mm and (c) R = 250 nm h_{water} = 3 mm, with initial water volume of 168 µL corresponding to a 3 mm height of water into the tank. Considering each box, the FSR slope of increased values stands as a specific signature of the phase 1, as a migration and sedimentation mechanisms of the NPs after impact of the NPs droplet as initial condition; the 'cloud' of NPs may be considered as a complex composite medium that have collapsed before migrating and moving on the flow of the vortex prior to sedimentation. The densification of this composite silica layer reduces the value of the effective group index of the resonant mode, yielding then the FSR increase. The peak of the values highlights the t_{phase1} instant at the end of the first phase, while the decreasing part of the curve corresponds to the second phase of rearrangement with the observed increase of the curvature of the air/water interface upstream. The last step, with steady FSR values, corresponds to a stable layer of nano-particles after end of sedimentation.

Fig. 6 shows a schematic illustration of the sedimentation of the NPs clouds in the aqueous fluid over time until the final stage of sedimentation marked by the deposit of the NPs at the bottom of the tank and thus on the resonant light circuit. The NPs cloud can be considered as a composite medium moving progressively towards the surface of the photonic chip. Spherical NPs in suspension sedimenting into water, aggregate by becoming denser above the resonators within the water fluid.

By way of example, Fig. 7 (a), (b) and (c) represent respectively the spectra at the three times t_1 = 1 min, t_2 = 30 min and t_3 = 140 min plus the associated Fast Fourier Transform (FFT) curves, during the process of sedimentation of a cloud of nano-particles with monodispersed diameter D = 600 nm. At the same time, the main part of the FFT curve is digitized by an interpolation of Lagrange based on parabolic type in view of the shape of FFT peaks. The diagram Fig. 7 (d) represents the synopsis of the method. Thus, from the numerical determination of the three parameters α,β and γ which represent the digitized FFT at the top (Lagrange's polynomial $\alpha.(x_{FSR})^2 + \beta,x_{FSR} + \gamma$), it is possible to determine such specific abscissa, namely the FSR. Fig. 7 (e) represents the schematic evolution of the FSR over time during all the experiments monitoring the dynamic process of sedimentation. I can be noted that the relative variation of the FSR varies from factor 1 to 1.4 during the process (Fig. 7 (d) between t_1 and t_3, with FSR-t_3 1.4 FSR-t_1). As shown in Fig. 7 (d), the maximum of the FFT curve is approximated by the Lagrange's interpolation and thus determined accurately in real time considering said interpolation presenting a single maximum value. During such a process The Matlab code and the man–machine interface specifically developed allow to draw the normalized FSR(t) curves directly onto the screen in real time. Fig. 8 (a), (b) and (c) illustrate the experimental time evolution of the normalized FSR during the dynamic sedimentation process for spherical silica NPs of different radii ($R_{particles}$ = 400, 300 and 250 nm), in an initial water volume of 168 µL corresponding to a water height of 3 mm directly on the device acting with its resonant signal. First, these graphs show a generic behavior of the evolution of the FSR as a function of time.

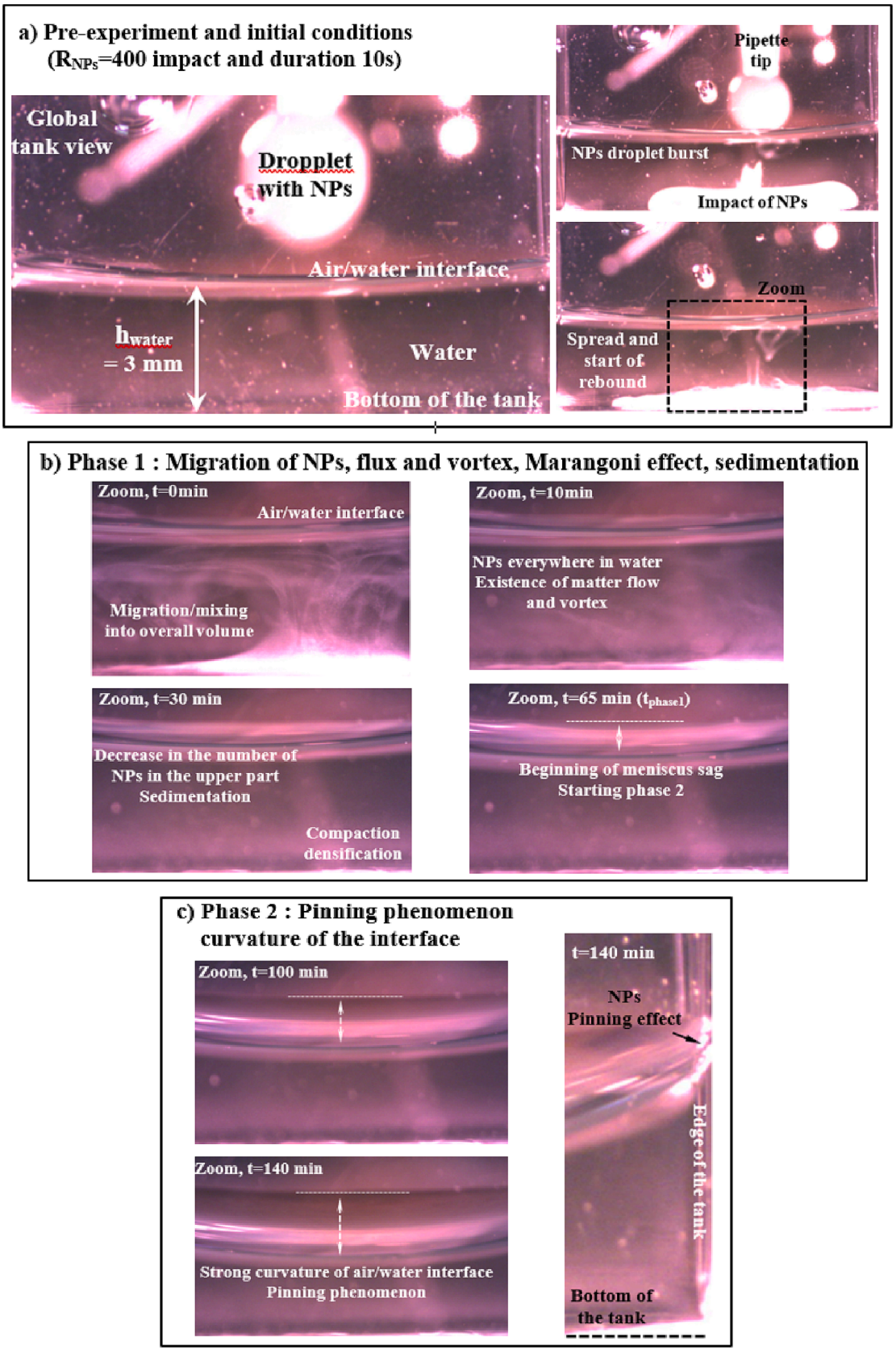

Fig. 9. Monitoring by way of optical volume imaging of the whole dynamic process ($R_{nanoparticles}$ = 400 nm): a) impact of the droplet with the NPs (initial conditions during a few seconds), b) phase 1 of migration of the NPs (with Marangoni effect) and sedimentation, then c) phase 2 with accentuation of the curvature of the air/water interface, most likely due to a pinning phenomenon at the triple point and edges of the tank.

Table 2
Theoretical sedimentation speed values for silica nano-particles (NPs) with radius 250, 300 and 400 nm in water according to the Stokes model (with $\eta = 1$ mPa.s, $\Delta\rho = \rho_{NP} - \rho_{water} = 2650–1000 = 1650$ kg/m^3 and $g = 9.81$ m/s^2), compared to average experimental sedimentation rate values obtained by measurements on resonant surface light probes. The parameter h_{water} represents the water height into the tank and t_{phase1} the phase 1 duration given by the instant t_{phase1} as the FSR(t_{phase1}) reaches its maximum value before decreasing under the resonant surface probe (Fig. 8).

Dimensions of the Nano-Particles (nm)	R-radius	250	300	400
Sedimentation Velocity (μm/min)	v_{Stokes} *Theoretical with Stokes formula*	13.5	19.4	34.5
	$\overline{v}_{phase1} = h_{water} / t_{phase1}$ *Average of Experimental with various h_{water} (2 and 3 mm)*	15.5	17.5	42.8
	Relative difference (%)	12.9	9.7	19.3

For each measurement, the slope of the increased FSR values stands as a specific signature of the sedimentation mechanism. FSR values increase fairly steadily until they reach a peak followed by a systematic decrease to a constant value. The whole set of experiments on a resonant surface regarding the FSR variation leads to a generic curve considering Fig. 7 (e) or experimental Fig. 8 (a), (b) and (c). Looking at the measurements under the resonant principle (Fig. 8), the identification of a specific time t_{phase1} is highlighted above all. Such a time is determined by what the probe detects, namely the characteristic times appearing on the FSR(t) variation curves. During this phase 1 (with duration t_{phase1}) the FSR is increased up to a maximum reaching typically 1.4 times its original value in our case (Table Fig. 7 (d), last line, Fig. 7 (e) plus Fig. 8); this is probably specific to the nature of the material considering the migrating NPs. In the theoretical framework of guided optics, the cloud of nanoparticles is equivalent to a layer of a composite medium whose refractive index is between that of water and silica. The sedimentation of this NPs cloud is then equivalent to an effective medium or dispersed cloud of a given index (lower than that of the guiding structure).

4.2. Optical imaging of the volume process: impact, migration plus sedimentation

A side camera (EO-2013C) is positioned to image and record, after the impact, the dynamic processes of migration of NPs and their sedimentation in the reservoir thanks to relevant photographs. Fig. 9 represents the monitoring of the impact as an initial condition, migration (starting at t = 0 min), and sedimentation: the whole process is followed by optical volume imaging for NPs with a radius of $R_{nanoparticles} = 400$ nm. Concerning the initial condition, the droplet containing the NPs bursts, causing then the NPs to diffuse within the entire volume (in a few seconds) followed by both migration and sedimentation phenomena. During migration, vortices and fluxes of NPs material can be distinguished while mixing. The Marangoni effect acts during this phase 1. Eventually, from the instant noted t_{phase1} (or end of phase 1, around 65 min for NPs with a radius of 400 nm) a second phase seems to set in: during the latter, a strong increase in the curvature of the air/water interface can be observed. Such a second phase appears clearly with the curvature of the meniscus of the upper air/water interface significantly increased on the optical images (Fig. 9 (c), t > 65 min). The triple points (or attachment points at the edges of the tank at the air/water interface) remain fixed, but at the center of the tank this interface and curvature collapse. This manifestation is similar to a pinning phenomenon which can be explained by NPs that have been identified and positioned at the triple points at the edges (interface air/water contact at the edges of the tank).

4.3. Discussions, interpretations and attempted corroboration

In terms of initial conditions, considering the optical volume imaging of the deposition process of the microdroplet containing the nanoparticles, it can be seen first of all that the penetration of the droplet within the water medium before reaching the bottom of the tank, entails a real impact prior to the release of the NPs. This also explains why experiments under resonant probes detect right from the start a variation of the FSR (at t = 0 min after the impact and the beginning of the migration). Upon impact, with the penetration and bursting of the microdroplet, a certain amount of NPs escapes from this source point. Then, during the first phase a migration of these nanoparticles may be considered in the whole volume with specific movement and vortex of this fragmented material after a form of bursting. It can be noted that the Marangoni effect (Marangoni, 1871; Le Roux, 2015; Miniewicz et al., 2019) sets in, due to the flow of matter (fluid plus nanoparticles): thus, while monitoring both processes of migration and then of sedimentation, oscillations of the FSR over time (Fig. 8) are observed. The complex circulation of the fragmented material or cloud of nanoparticles is the main cause. Moreover, after migration and during the sedimentation process of the cloud, due to the geometry of the non-infinite tank (with its edges and angles, then its upper surface subject to evaporation), others concentration gradients and surface tensions trigger an additional small circulation of the fragmented material in its own volume. Thus, mini-currents and interactions can always be found within such complex deformable cloud fragmented into NPs. During this first phase 1, the carpet of NPs having reached the bottom of the tank forms a more compact layer; the density or concentrations of silica NPs is thus increased.

Thus, considering the signal resonance (Fig. 8) after impact, during this first phase of migration then sedimentation of NPs, the FSR shows an increase until a certain time t_{phase1} marking the end of migration/sedimentation. The evolution of the FSR quantity can be interpreted as follows: during the phase of symmetrization of the guidance structure, both lower and upper optical cladding become identical and the guiding capacity is somewhat increased. A densification plus 'compactus', leading to a statistical increase in the density of the silica material $\Delta\rho$ (above the MRs) will act; the so-called Gladstone macroscopic law will couple and allow for the FSR change: it will then acting onto the Stokes law: $v_{Stokes} = \frac{2}{9}\frac{gR^2(\rho_{NP}-\rho_{water})}{\eta_{water}} = \text{cste}.R^2(\Delta\rho)$. This Gladstone's law on the optical index *n* concern all known materials, positing that $(n-1)/\rho = \text{cste}$, with ρ the density of the material. Then, during the second step with the sedimentation or densification $\Delta\rho$, the so-called macroscopic law of Gladstone imposes also a related variation of the optical index $\Delta n \propto \Delta\rho$. With the resonant light configuration quantified by $FSR = \frac{\lambda_0^2}{P.n_{eff}^{group}}$, a direct proportionality is imposed between $\Delta\rho$ and the variation of the ΔFSR. Thus, as the group index n_{eff}^{group} of the light decreases, the FSR value will rise over time. Then, after the migration of NPs into the whole volume and the approach of the cloud of fragmented matter, an accumulation of silica NPs appears gradually above the sensing device (with the resonant signal). The statistical density of the area specific to the silica material is increased during the end of phase 1. The duration t_{phase1} of the FSR growing can be associated to the deposition of the nanoparticle cloud onto the active surface, the instant t_{phase1} being materialized by the peak of the curve on Fig. 8.

In addition, we can try to compare and link this characteristic time (from the resonant probes), with the simple Stokes model: the quotient (h_{water}/t_{phase1}) is naturally calculated as an average velocity $\overline{v}_{phase1}$ of the complete process, namely migration then sedimentation with phase 1. Table 2 compares the theoretical values of the sedimentation velocity (NPs of respective radius; 250, 300 and 400 nm in water according to the Stokes model with: $\eta_{water} = 1$ mPa.s, $\Delta\rho = \rho_{NP} - \rho_{water} = 1650$ kg/m^3 and $g = 9.81$ m/s^2), with the average experimental values of the $\overline{v}_{phase1}$ velocity obtained by measurements with the resonant surface light probes.

Thus, this comparison related to the classical Stokes model highlights in a strange way a relative correspondence of the values observed between 9 and 19%. Therefore, this model, although simple, is interesting for a first estimation of the global phenomenon including; impact plus migration and sedimentation. Indeed, it is hypothetically reduced to the behavior of a single spherical particle in the aqueous medium.

5. Conclusion

This paper presents a study of the behavior of a resonant optical signal generated onto an acting surface, the device involving integrated photonics to constitute a probe dedicated to the detection of migration of a cloud of nanoparticles (NPs) plus a sedimentation process. Thus, appropriate measurements of the serial migration/sedimentation dynamic processes of NPs in a reservoir containing a fluid are achieved from the transduced signal. These types of processes belonging to the soft matter and fragmented matter domain are investigated by means of micro-technologies and specific materials: thus, the realized surface photonic probes are based on waveguides, tapers and a set of four distributed resonators. The whole structure hinges on a sensing device whose fabrication requires adequate thin layers processes, overlaid with a millimeter tank. So as to achieve relevant measurements, a whole set of optoelectronics has been designed and a specific signal processing approach has been developed. These measurements are based on the dynamic evolution of the period of the spectra (or FSR) as a function of time considering the resonant signals and there real time treatment. In fact, we have verified the practicability of an efficient detection by a quasi-surface technology with evanescent resonant guided light without the need of a volume technology: To substantiate this, several dynamic migration and sedimentation measurements have been performed with three types of silica NPs of different radii. First, it appears that these probes can detect the whole behavior of each process by providing specific and generic curves on the dynamic monitoring of the resonant parameter FSR. Such curves clearly show different phases, namely: the detection after the impact of the migration and sedimentation or approach of the nanoparticles cloud above the resonant light surface, an increase in density and concentration of these nanoparticles above the surface, then a definite contact followed by a phase of rearrangement of the nanoparticles on the surface for a deposit stabilizing at the end. Therefore, in our resonant experiments the time t_{phase1} appears naturally as a detectable characteristic for the curves (provided by the resonant probes), considering the maximum value of the observed FSR. In addition, another visible mechanism (that we called phase 2) appears in the volume imaging experience, as regards the increase in the curvature of the air/water interface with an attachment to the walls of the tank and the pinning phenomenon. For such a second phase the FSR decreases before stabilizing: this is due to a highly visible pinning phenomenon of the NPs remaining at the air/water/tank edge interface, then modifying the conditions at the triple point and strongly accentuating the curvature (or meniscus) of the interface.

Considering the set of generic curves describing the resonant signal, the end of migration of the squeezed cloud can be identified by the end t_{phase1} of phase 1. This characteristic time makes it possible to define the $\overline{v}_{phase1}$ velocity and to compare it with the so-called Stokes velocity. The observed discrepancies (between 9 and 19 %), can be explained by the complexity of the fragmentary nature of the sedimentary cloud after the impact and migration. This work constitutes a first result on the monitoring of NPs migration under a resonant signal, since the concentration values occurring in the entire volume of water in the reservoir remain low: indeed rheology measurements have confirmed that it is not necessary to take into account an effective viscosity η_{eff}. However it is possible that at the end of the migrations of NPs other models should be considered, due to the high concentrations confined in a smaller volume (Richardson and Zaki, 1954; Le Roux, 2015). Our approach can therefore find advantageous applications in galenic pharmacology and specific food industry for quality control: one can indeed consider lotions whose active ingredient is in colloidal suspension before sedimentation when the substance expires.

Declaration of Competing Interest

The authors declare the following financial interests/personal relationships which may be considered as potential competing interests: Bruno BECHE reports financial support was provided by Institute of Electronics and Telecommunications of Rennes. Bruno BECHE has patent Method for determining a sedimentation or creaming rate issued to PCT/EP2019/051103 U.S. Application Number n 16/966,416.

Data availability

No data was used for the research described in the article.

Acknowledgment

The authors thank the “Fondation d’Entreprise Grand Ouest” (BPGO) plus the Fondation Rennes1 of the university of Rennes for its financial support of this work and the NanoRennes platform for the DUV process (https://www.ietr.fr/en/nr-nanorennes-platform). This study is also a part of a PASS_programm ‘cordée de la réussite’ named ‘Pour une Ambition Scolaire Scientifique’ (For a Scientific School Ambition) with the Brittany center (Sir Cyril Le-Corre and Madame Valérie Mesnet at Lycée Fulgence Bienvenüe, and Collèges Louis Guilloux, Paul Eluard, Romain Rolland, https://spm.univ-rennes1.fr/les-cordees-de-la-reussite). The authors would like to thank Pascal Panizza, Professor at the University of Rennes for his discussions in fluid mechanics.

References

Aidi, M., Feuillebois, F., Lasek, A., Anthore, R., Petipas, C., Auvray, X., 1989. Mesure de la vitesse de sedimentation d’une suspension par absorption de rayon X. Revue Phys. Appl. 24, 1077–1084.
Bissig, H., Romer, S., Cipelletti, L., Trappe, V., Schurtenberger, P., 2003. Intermittent dynamics and hyper-aging in dense colloidal gels. Phys. Chem. Comm. 6, 21–23.
Blazy, P., Jdid, E.A., Bersillon, J.L., 1999. Décantation Aspects théoriques. Techniques de l’Ingénieur J 3450, 1–10.
Blazy, P., Jousset, R., 2011. Classification hydraulique en dimensions - Classification par sédimentation. Techniques de l’Ingénieur J 3131, 1–12.
Cabane, B., Hénon, S., 2007. Liquides: solutions, dispersions, émulsions, gels, Belin Paris.
Castro-Beltrán, R., Huby, N., Vié, V., Lhermite, H., Camberlein, L., Gaviot, E., Bêche, B., 2015. A laterally coupled UV210 polymer racetrack micro-resonator for thermal tenability and glucose sensing capability. Adv. Dev. Mat. 1, 80–87.
Castro-Beltrán, R., Garnier, L., Saint-Jalmes, A., Lhermite, H., Cormerais, H., Fameau, A. L., Gicquel, E., Bêche, B., 2020. Microphotonics for monitoring the supramolecular thermoresponsive behavior of fatty acid surfactant solutions. Opt. Commun. 468, 125773.1-7.
Chao, C.Y., Fung, W., Guo, L.J., 2006. Polymer microring resonators for biochemical sensing applications. IEEE J. Sel. Top. Quantum Electron. 12, 134–142.
Cipelletti, L., Ramos, L., 2002. Slow dynamics in glasses, gels and foams. Curr. Opin. Colloid Interface Sci. 12, 23–28.
De Gennes, P.G., Brochard-Wyart, F., Quéré, D., 2005. Gouttes, bulles perles et ondes, Belin Paris.
Delezoide, C., 2012. Polymer microring resonators for optofluidic evanescent field sensors (Ph.D. thesis). University of Paris-Saclay / ENS.
Delezoide, C., Salsac, M., Lautru, J., Leh, H., Nogues, C., Zyss, J., Buckle, M., Ledoux-Rak, I., Nguyen, C.T., 2012. Vertically coupled polymer microracetrack resonators for label-free biochemical sensors. Photon. Technol. Lett 24, 270–272.
Duval, D., Lhermite, H., Godet, C., Huby, N., Bêche, B., 2010. Fabrication and optical characterization of sub-micronic waveguide structures on UV210 polymer. J. Opt. 12 (055501–1), 055501–055506.
Anton Paar GmbH, Rhéomètre https://www.anton-paar.com/fr-fr/produits/groupe/rheometre/, 2022.
Hallil, H., Dejous, C., Hage-Ali, S., Elmazria, O., Rossignol, J., Stuerga, D., Talbi, A., Mazzamurro, A., Joubert, P.Y., Lefeuvre, E., 2021. Passive resonant sensors: trends and future prospects. IEEE Sens. J. 21, 12618–12632.
Lanotte, L., Boissel, F., Shuck, P., Jeantet, R., Le Floch-Fouéré, C., 2018. Drying-induced mechanisms of skin formation in mixtures of high protein dairy powders. Colloids Surf. A 553, 20–27.
Le Floch-Fouéré, C., Lanotte, L., Jeantet, R., Pauchard, L., 2019. The solute mechanical properties impact on the drying of dairy and model colloidal systems. Soft Matter 15, 6190–6199.
Le Roux, S., 2015. Effet Marangoni aux interfaces fluides (Ph.D. thesis). University of Rennes.

Li, Q., Vié, V., Lhermite, H., Gaviot, E., Bourlieu, C., Moréac, A., Morineau, D., Dupont, D., Beaufils, S., Bêche, B., 2017. Polymer resonators sensors for detection of sphingolipid gel/fluid phase transition and melting temperature measurements. Sens. Actuators A 263, 710–717.

Manley, S., Davidovitch, B., Davies, N.R., Cipelletti, L., Bailey, A.E., Christianson, R.J., Gasser, U., Prasard, V., Segre, P.N., Doherty, M.P., Sankaran, S., Jankovsky, A.L., Shiley, B., Bowen, J., Eggers, J., Kurta, C., Lorik, T., Weitz, D.A., 2005. Time-dependent strength of colloidal gels. Phys. Rev. Lett. 95 (048302–1), 048302–048304.

Marangoni, C., 1871. Sul principio della viscosita superficiale dei liquidi stabiliti dalsig. j. plateau. Il Nuovo Cimento Series 2 (5–6), 239–273.

Meziane, F., Raimbault, V., Hallil, H., Joly, S., Conédéra, V., Lachaud, J.L., Béchou, L., Rebière, D., Dejous, C., 2015. Study of a polymer optical microring resonator for hexavalent chromium sensing. Sens. Actuators B 209, 1049–1056.

Midelet, J., El-Sagheer, A., Brown, T., Kanaras, A., Werts, M.H.V., 2017. The sedimentation of colloidal nanoparticles in solution and its study using quantitative digital photography. Part. Part. Syst. Charact. 34.

Miniewicz, A., Bartkiewicz, S., Karpinski, P., 2019. Optical trapping mechanisms based on optothermal Marangoni effect, Proc. SPIE 11083. Optical Trapping and Optical Micromanipulation XVI 11083, 1–6.

Nam, K.H., Yeom, E., Ha, H., Lee, S.J., 2012. Simultaneous measurement of red blood cell aggregation and whole blood coagulation using high-frequency ultrasound. Ultrasound Med. Biol. 38, 468–475.

Pelletier, C., 2009. Mesures de turbidité. Techniques de l'Ingénieur R 2355, 1–19.

Qavi, A.J., Bailey, R., 2010. Multiplexed detection and label-free quantitation of microRNAs using arrays of silicon photonic microring resonators. Angew. Chem. Int. Ed. 49, 4608–4611.

Qavi, A.J., Kindt, J.T., Gleeson, M.A., Bailey, R.C., 2011. Anti-DNA:RNA antibodies and silicon photonic microring resonators: increased sensitivity for multiplexed microRNA detection. Anal. Chem. 83, 5949–5956.

Rabiei, P., Steier, W.H., Zhang, C., Dalton, L.R., 2002. Polymer Micro-Ring Filters and Modulators. J. Lightwave Technol. 20, 1968–1975.

Rabus, D.G., 2007. Integrated Ring Resonators the Compendium. Springer, New York.

Razavian, S.M., Wenby, R.B., Fisher, T.C., Meiselman, H.J., 1997. Determination of particle sedimentation rate by ultrasonic interferometry: role of particle size, density and volume fraction. Biorheology 34, 349–362.

Reynoso-De La Cruz, H.M., Ortiz-Ricardo, E., Camarena-Chavez, V.A., Martinez-Borquez, A., Gutierrez-Juarez, G., U'Ren, A.B., Castro-Beltran, R., 2021. Low-cost fabrication of microlasers based on polymeric micropedestals. Appl. Opt. 60, 720–726.

Richardson, J.F., Zaki, W.N., 1954. Sedimentation and fluidization. Part 1. Trans. Inst. Chem. Eng. 32, 35–53.

Rohm and Haas Electronic Materials, UV 210 Positive photoresist, https://kayakuam.com/products/uv-210gs-positive-duv-photoresist/, Kayaku Advanced Materials Inc.'s, 2005.

Schweinsberg, A., Hocdé, S., Lepeshkin, N.N., Boyd, R.B., Chase, C., Fajardo, J.E., 2006. An environmental sensor based on an integrated optical whispering gallery mode disk resonator. Sens. Actuators B 123, 727–732.

Stokes, G.G., 1851. On the effect of the internal friction of fluids on the motion of pendulums. Philos. Mag. 1, 337–339.

Su, J., 2015. Label-Free Single Exosome Detection Using Frequency-Locked Microtoroid Optical Resonators. ACS Photon. 2, 1241–1245.

Tee, S.Y., Mucha, P.J., Cipelletti, L., Manley, S., Brenner, M.P., Segre, P.N., Weitz, D.A., 2002. Nonuniversal velocity fluctuations of sedimenting particles. Phys. Rev. Lett. 89, 054501.1-4.

Vollmer, F., Arnold, S., 2008. Whispering-gallery-mode biosensing: label-free detection down to single molecules. Nat. Meth. 5, 591–596.

Xu, D.X., Vachon, M., Densmore, A., Ma, R., Janz, S., Delâge, A., Lapointe, J., Cheben, P., Schmid, J.H., Post, E., Messaoudene, S., Fédéli, J.M., 2010. Real-time cancellation of temperature induced resonance shifts in SOI wire waveguide ring resonator label-free biosensor arrays. Opt. Express 18, 22867–22879.

Yu, M., Le Floch-Fouéré, C., Pauchard, L., Boissel, F., Fu, N., Chen, X.D., Saint-Jalmes, A., Jeantet, R., Lanotte, L., 2021. Skin layer stratification in drying droplets of dairy colloids. Colloids Surf. A 620, 126560.1-9.